Weak localization in graphene flakes: supplementary material

F. V. Tikhonenko, D. W. Horsell, R. V. Gorbachev, and A. K. Savchenko

School of Physics, University of Exeter, Stocker Road, Exeter, EX4 4QL, U.K.

Samples

Samples were manufactured using the method of mechanical exfoliation of highly-oriented pyrolytic graphite devised in [1], on a n^+Si/SiO_2 substrate with oxide layer of thickness $t = 300\,\mathrm{nm}$. Lithographically defined Au/Cr contacts were subsequently made to each flake. Resistance measurements were carried out in the temperature range from 0.25 to 25 K using a standard lock-in technique with 1 nA driving current. Samples B, D, F1 are two-terminal and F2 is four-terminal (the additional contacts were used to account for the contact resistance). The concentration of carriers (electrons n and holes p) in graphene is determined by the capacitance between the graphene and n^+Si substrate: $e(p-n) = (\epsilon\epsilon_0/t)V_g$. There was a small unintentional doping of the samples leading to a shift in gate voltage ($\sim 5\,\mathrm{V}$) of the position of the resistance peak with respect to $V_g = 0$, which has been accounted for in the main text. The graphene–Au/Cr contact resistance has been found from the deviation of the height of the quantum Hall plateau from the expected value of $2e^2/h$ (see insets to Fig. 1 of main text). The values of the contact resistance for samples F1 and D are about $\sim 100\,\Omega$ and $\sim 600\,\Omega$ for sample B.

Averaging procedure and analysis of magnetoconductance

A method of effective averaging is important in small-sized samples to remove the influence of mesoscopic fluctuations, as without it one can get contradictory results for the magnetoconductance (MC). (If we attempt to measure $\Delta\sigma(B)$ at different V_g, the character of the MC depends on the specific point in V_g at which it is measured). Figure 1 shows how the averaging is performed. For each temperature the conductivity of the sample as a function of the gate voltage is first measured across a 2 V range at incremental values of the magnetic field. Then the curve at zero magnetic field is subtracted from each curve and the resulting difference is averaged across the 2 V gate voltage range. One can see from Fig. 1 the average increase of $\langle\Delta\sigma\rangle_{\Delta V_g}$ with magnetic field. These averaged values of the MC are plotted as a function of B in Figure 2 of the main text.

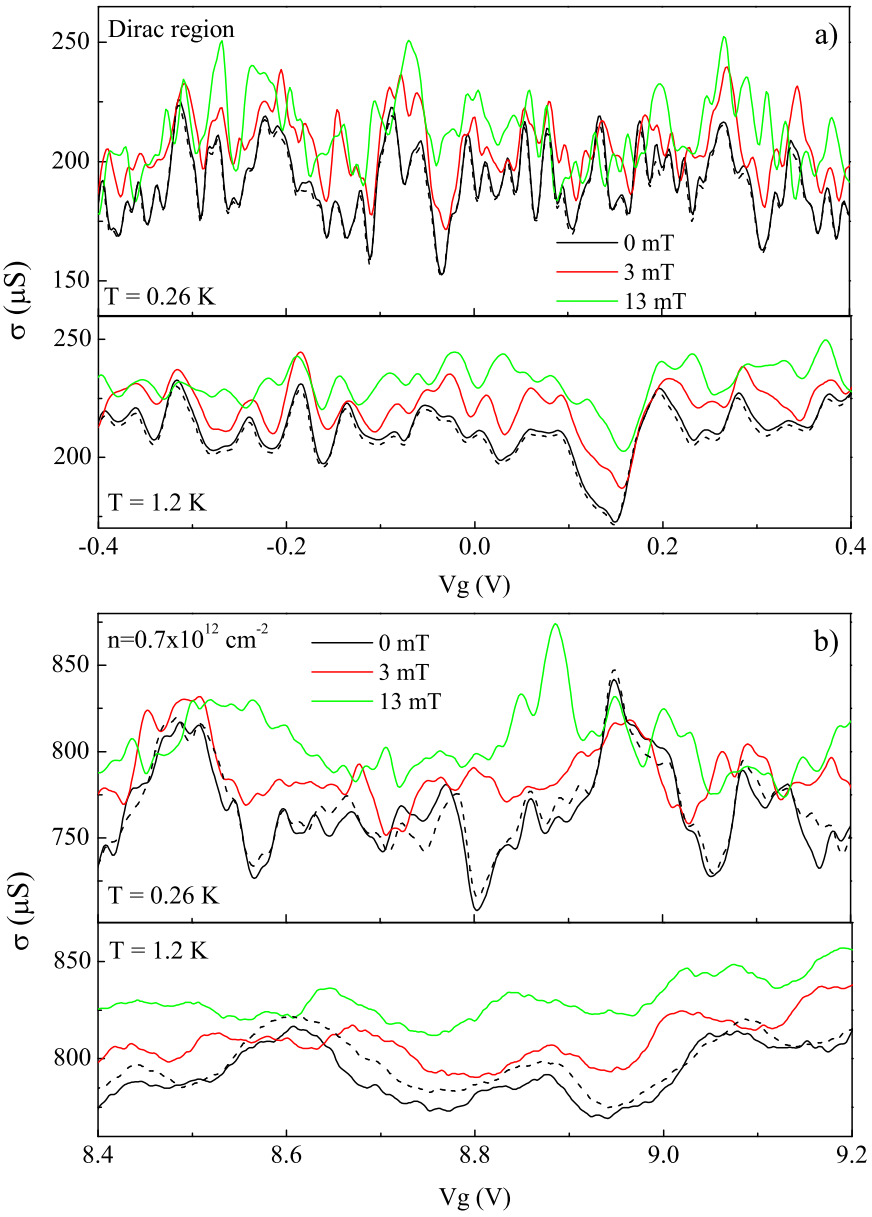

FIG. 1: Illustration of the averaging procedure of the magnetoconductance of sample F1 in two density regions at two temperatures (only a fraction of ΔV_g is shown here): (a) Dirac region, (b) electron region. Dotted lines show repeated sweeps at $B = 0$.

The perturbation theory of weak localization (WL) is applicable at $k_F l \gg 1$ (a diffusive metal). In our samples $k_F l$, found from the conductivity $\sigma = 2e^2(k_F l)/h$, varies in the range 3–30, with the smallest values in the Dirac region: 4, 3, 8 and 6 for samples D, F1, F2 and B, respectively. Another limitation for the application of the diffusive theory of WL is $B \lesssim B_{\rm tr}$, where the 'transport' magnetic field is found from the condition $L_B = (\hbar/eB)^{1/2} \approx l$. This

limits the range of magnetic fields where we perform the analysis to $B \leqslant 100\,\mathrm{mT}$.

For the narrowest sample B, the dephasing length is larger than its width and therefore the 1D theory of WL [2] should be used in the analysis of its MC in small fields. However, at fields where $L_B < W$ (W is the width of the sample) i.e. at $B > 7$ mT, the 2D theory becomes applicable. As the bulk of the data is obtained in this range of the field, we have used 2D theory (Eq. 1 in main text) to analyse the MC.

Comparison of characteristic lengths and times

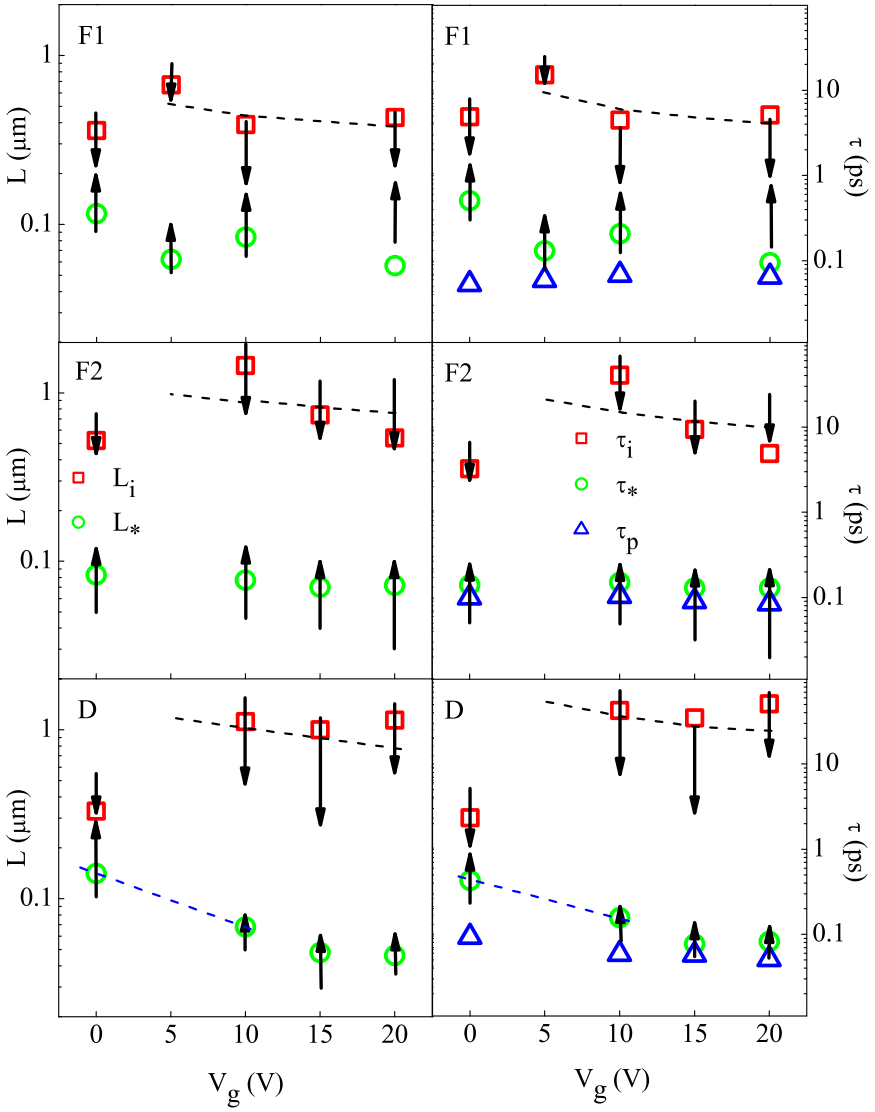

FIG. 2: Comparison of characteristic lengths and times for samples F1, F2 and D at different carrier densities.

Figure 2 shows for samples F1, F2 and D a comparison of the length L_* with length L_i,

as well as the values of the corresponding times τ_* and τ_i (using $L_x = (D\tau_x)^{1/2}$) for different carrier densities. We emphasise that in the analysis of the MC the value of L_* is closely linked to that of L_i. In Eq. 1 the second and third terms have the same sign, therefore by a slight increase of one of them and a corresponding decrease of the other, one can get a similar agreement with experiment. Figure 2 shows not only the values found from the best fit (the higher B-region being most sensitive to these two parameters) but also the synchronous variation allowed in these values while retaining a good fit, indicated by arrows. In spite of the variations, there are several trends seen in the figure. First, the value of L_i is always significantly larger than L_* and somewhat larger in the better quality sample F2. Second, there is a decrease of L_i with increasing carrier density, although its value is smaller in the Dirac region. Finally, there is a decrease of L_* when the carrier density is increased above the Dirac region. The dashed curves in Fig. 2 indicate the expected decrease of L_i and τ_i if the scattering rate is proportional to the density of states, which increases linearly with the Fermi energy $\epsilon_F \propto V_g^{1/2}$.

Estimations of the effects suppressing WL in a single valley

Trigonal warping

According to [2] the breaking of the time-reversal symmetry in one valley can occur due to the suppression of backscattering by the trigonal warping of the Fermi surface. The trigonal warping rate is

$$\tau_w^{-1} = 2\tau_p(\mu\epsilon_F^2/\hbar v_F^2)^2 \ ,$$

where τ_p is the momentum relaxation time, $v_F \approx 10^6\,\mathrm{ms}^{-1}$ is the Fermi velocity and μ is the structural parameter equal to $\mu = \gamma_0 a^2/8\hbar^2$. Here $\gamma_0 \approx 3\,\mathrm{eV}$ is the nearest-neighbour hopping energy and $a \approx 0.26\,\mathrm{nm}$ is the lattice constant in graphene. For the typical parameters in our samples we obtain $\tau_w^{-1} \approx 0.001\,\mathrm{ps}^{-1}$ for the Dirac region ($\epsilon_F \approx 30\,\mathrm{meV}$, $\tau_p \approx 0.1\,\mathrm{ps}$) and $\tau_w^{-1} \approx 0.3\,\mathrm{ps}^{-1}$ for the highest measured concentration ($\epsilon_F \approx 130\,\mathrm{meV}$, $\tau_p \approx 0.05\,\mathrm{ps}$). Trigonal warping of the Fermi surface is therefore a very weak effect compared to other intra-valley scattering mechanisms and cannot be the main reason of the strong chirality-breaking observed in our experiments ($\tau_*^{-1} \approx \tau_p^{-1}$).

Dislocations

Another possible mechanism of chirality breaking in the graphene sheet is dislocations in the honeycomb lattice [3]. If the trajectory of a quasiparticle goes near the core of a

dislocation it leads to a change of the phase due to the induced strain. For randomly distributed dislocations the scattering rate related to this mechanism is

$$\tau_{\text{gauge}}^{-1} \approx \frac{v_F}{k_F \xi^2} ,$$

where ξ is the average distance between dislocations [3]. In order to obtain the experimentally found chirality-breaking rate $\tau_*^{-1} \approx 10$ – $20\,\text{ps}^{-1}$ the distance ξ should be about $15 - 50\,\text{nm}$. However, the cores of the dislocations should also cause inter-valley scattering, which is why this estimation is in contradiction with the relatively large value of the inter-valley scattering length ($L_i \approx 1\mu\text{m}$) observed experimentally.

Ripples

As proposed in [4], ripples in the graphene layer on a silica substrate can lead to suppression of weak localization because of the effective magnetic field generated by strain of the interatomic bonds. The vector potential corresponding to a single ripple with diameter d and height h is [4]:

$$A = \frac{\gamma_0 \left|\nabla h\right|^2}{e v_F} ,$$

where $\nabla h \approx h/d$. The flux through one ripple is $\Phi = \oint \mathbf{A} \cdot \mathrm{d}\mathbf{l} \approx Ad$ and $\Phi = \int \mathbf{B} \cdot \mathrm{d}\mathbf{S} \approx Bd^2$, therefore the magnetic field associated with one ripple is

$$B \approx \frac{A}{d} = \frac{\gamma_0}{e v_F} \frac{h^2}{d^3} .$$

Since the curvature vector of a ripple is random, the resulting magnetic field through the area limited by the dephasing length L_ϕ and containing $N \approx L_\phi^2/d^2$ ripples should be averaged as follows:

$$B_{\text{eff}} = \frac{B}{\sqrt{N}} = \frac{\gamma_0}{e v_F L_\phi} \left(\frac{h}{d}\right)^2 .$$

The roughness of the graphene sheet found from AFM measurements is about 0.3 nm and the size of the features is about 10 nm. This gives a value for the magnetic field associated with one ripple $B \sim 0.1\,\text{T}$. For our typical value of $L_\phi \sim 1\,\mu\text{m}$ the effective magnetic field is then $B_{\text{eff}} \sim 1\,\text{mT}$. Since suppression of the quantum interference requires a magnetic field $B_{\text{eff}} > B_{\text{tr}} \sim 0.1\,\text{T}$, the estimated value is too small to destroy the localization effect. The random magnetic field can only introduce an uncertainty in the value of B, Fig. 2 of the main text, comparable to the accuracy to which the field is set by the power supply.

Potential gradients

The last mechanism which can produce the breaking of time-reversal symmetry is a gradient of potential coming from the charged impurities in the substrate. A potential gradient leads to a distortion of the dispersion curve of a single valley and hence breaks the valley symmetry. As shown in [3] the resulting scattering rate can be estimated as

$$\tau_{\mathrm{grad}}^{-1} \approx \tau_p^{-1} \left(k_F a\right)^2 \ .$$

In order to get $\tau_{\mathrm{grad}}^{-1} \approx \tau_p^{-1}$ one should have $k_F a \approx 1$. This corresponds to the carrier density $n = k_F^2/\pi \approx 5 \cdot 10^{14}\,\mathrm{cm}^{-2}$, which is two orders of magnitude higher than the densities studied in the experiment.

We conclude from these calculations that all existing estimations for the chirality-breaking scattering rates are not sufficient to explain our experimental results.

Scanning probe microscopy studies

The atomic force microscope used in this work was an Ntegra Aura from NT-MDT. We used non-contact tips NSG01 with resonance of 150 Hz at an amplitude of $\lesssim 40\,\mathrm{nm}$. To obtain high resolution in the xy-plane 'diamond-like carbon' coated tips with curvature radius $1 - 3\,\mathrm{nm}$ were used; tip convolution therefore limited feature resolution to this scale. To remove the influence of the water layer present on the silica substrate all measurements were performed in an atmosphere of dry nitrogen at 3 mbar, giving a tip resonance quality factor $Q \approx 1000$. The noise in the z-scale (height) is of the order 0.02 nm measured on pure graphite and silica with the AFM operating with acoustic and vibrational isolation.

We found that the surfaces of the silica and the graphene after lithographic processing were covered in droplets of PMMA with height $\approx 2\,\mathrm{nm}$, similar to the findings of [6]. They reduced the image quality and also made determination of the step edge between graphene and silica difficult. To obtain the scans of clean graphene shown in Fig. 4 of the main text we mechanically cleaned the surfaces. Figure 3(a) shows a phase contrast image of sample F2 where both the PMMA droplets and a cleaned area are seen.

To understand the extent to which the PMMA droplets exist under the flake (due to the lithographic process of depositing location markers prior to the deposition of the graphene flake), we introduced a tear and fold into the sample F2 as seen in Fig. 3(b). We see first that the surface under the flake is indeed free from PMMA droplets and therefore the topography of the flake is only influenced by the silica roughness. (This conclusion was

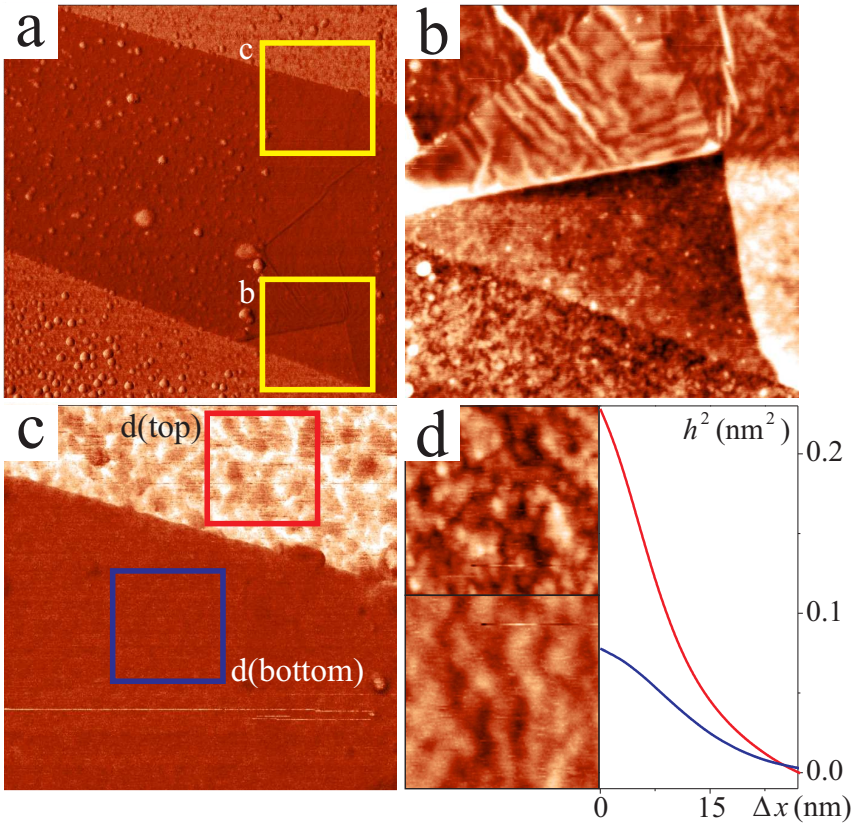

FIG. 3: AFM measurements of sample F2. (a) Phase contrast image where the PMMA droplets on the left and cleaned area on the right can be seen, with two regions in the clean area highlighted by boxes. (b) Magnified topographic image of box '(b)' showing the torn edge of the graphene flake. (c) Magnified phase contrast image of box '(c)' with silica (top) and graphene (bottom). (d) Autocorrelation analysis of the roughness in the boxes highlighted in (c), with insets of silica (top) and graphene topography (bottom). Scan (a) is 3 μm size and the phase change at the graphene–silica boundary is 2°. Scans (b)–(c) have the same 0.8 μm size. In (b) the colour-scale varies over 4 nm.

also confirmed by similar measurements on other flakes). Having a flake fold allows us to determine better the thickness of the flake, by measuring the step height between two graphene areas (as opposed to measurements of the step height between silica and graphene which always give a larger value of the step, ~ 1 nm). We find that the thickness of the flake is < 0.5 nm, which confirms that the flake is a monolayer (supporting the results of the quantum Hall measurements discussed in the main text). An interesting result from the tear is that the graphene flake has a tendency to form larger ripples when detached from the

silica surface, with a ripple height $\sim 0.5\,$nm and width 20 nm. (The roughness of the flake on the substrate is $\sim 0.3\,$nm, see the main text.) When comparing the surface roughness of silica and graphene, Fig. 3(c,d), we see that the surface height variation on the clean silica surface is $\sim 60\%$ larger than on the graphene, i.e. graphene significantly smoothes out the substrate roughness.

[1] K. S. Novoselov *et al.*, Science **306**, 666 (2004).

[2] E. McCann, *et al.*, Phys. Rev. Lett. 97, 146805 (2006).

[3] A. F. Morpurgo, and F. Guinea, Phys. Rev. Lett. **97**, 196804 (2006).

[4] S.V. Morozov *et al.*, Phys. Rev. Lett. **97**, 016801 (2006).

[5] R. V. Gorbachev *et al.*, Phys. Rev. Lett. **98**, 176805 (2007).

[6] M. Ishigami *et al.*, Nano Lett. **6**, 1643 (2007).